Laser ultrasonic imaging of complex defects with full-matrix capture and deep-learning extraction

Yujian Mei [a], Jian Chen [a,*], Yike Zeng [a], Lu Wu [a], Zheng Fan [b]

[a] *The State Key Laboratory of Fluid Power and Mechatronic Systems, School of Mechanical Engineering, Zhejiang University, Hangzhou 310027, China*
[b] *School of Mechanical and Aerospace Engineering, Nanyang Technological University, 50 Nanyang Avenue, Singapore 639798, Singapore*

ARTICLE INFO

ABSTRACT

Phased array-based full-matrix ultrasonic imaging has been the golden standard for the non-destructive evaluation of critical components. However, the piezoelectric phased array cannot be applied in hazardous environments and online monitoring due to its couplant requirement. The laser ultrasonic technique can readily address these challenging tasks via fully non-contact inspection, but low detection sensitivity and complicated wave mode conversion hamper its practical applications. The laser-induced full-matrix ultrasonic imaging of complex defects was displayed in this study. Full matrix data acquisition and deep learning method were adapted to the laser ultrasonic technique to overcome the existing challenges. For proof-of-concept demonstrations, simulations and experiments were conducted on an aluminum sample with representative defects. Numerical and experimental results showed good agreement, revealing the excellent imaging performance of proposed method. Compared with the total focusing model based on ray-trace model, the deep learning method could create superior images with additional quantitative information through end-to-end networks, which use the hierarchical features and generate details from all the relevant imaging and physical characteristics information. The proposed method may help assess defect formation and development at the early stage in a hazardous environment and understand the in-situ manufacturing process due to its couplant-free nature.

1. Introduction

Ultrasonic imaging is a powerful tool for identifying defects in the opaque materials, such as voids, delaminations, and anomalies, due to its noninvasiveness, deep penetration, and high accuracy [1,2]. Therefore, ultrasonic imaging has found numerous applications; for example, non-destructive evaluation (NDE) and structural health monitoring of critical components for the safety assurance in various fields, including aerospace planes, power plants, and civil structures [2–4]. Piezoelectric transducers are conventionally used to generate emitting ultrasonic waves and simultaneously detect the backscattered waves from the targets. Undoubtedly, considerable success has been achieved with this technique. However, piezoelectric transducers usually require a couplant, mostly water or gel. Therefore, such an imaging modality faces difficult challenges and even occasionally fails in certain scenarios, such as the in-situ monitoring of 3D printing and the online inspection of high-temperature or rotating objects.

Alternatively, as another important member of the ultrasound family, the laser ultrasonic technique (LUT) can overcome these challenges

due to its fully non-contact nature in generating and detecting ultrasonic waves [5–7]. Furthermore, LUT can yield high spatial resolution on the scale of optical wavelength and simultaneously excite multiple probing waves [5,8]. Consequently, LUT plays an important role in the fields where piezoelectric counterparts cannot work. Notably, LUT also features a few inherent disadvantages, such as weak generation, low detection sensitivity, and complicated setup, despite its considerable potential; all these disadvantages hamper its widespread use in practical applications. In particular, the ultrasonic waves should be generated in the thermoelastic regime considering NDE, under which the energy density of the generation laser must be kept below the damage threshold of the material under inspection. While these waves are weak to be detected [9], the low sensitivity of optical detection further deteriorates the performance [10–12]. A feasible solution is to collect and post-process enormous data to overcome these difficulties. For example, a large data collection method, namely full matrix capture (FMC), is widely applied in ultrasonic imaging, which acquires the waveforms by a phased array with all transmitter–receiver pairs [13,14]. Several well-established post-processing algorithms based on the acquired FMC data,
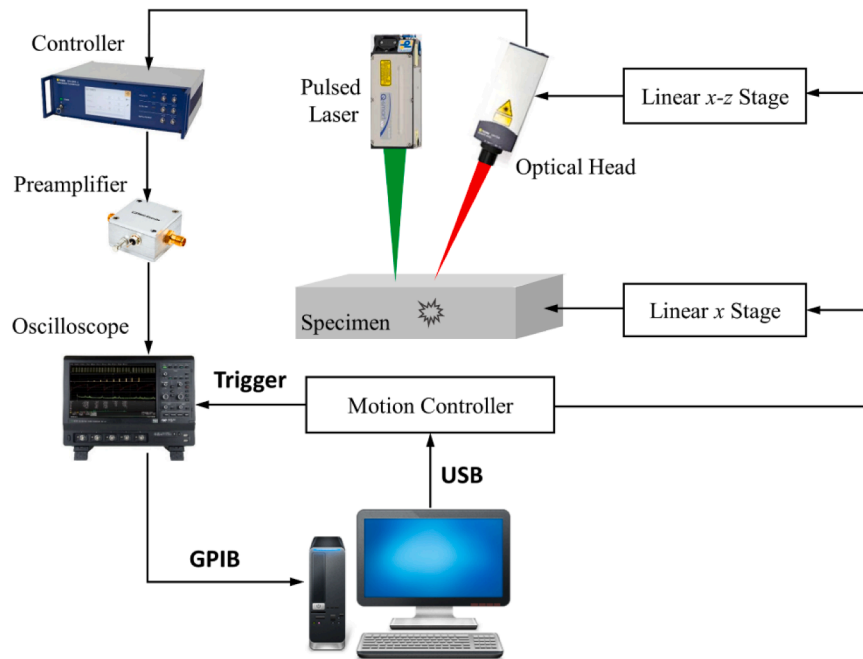
Fig. 1. Schematic diagram of the all-optical laser ultrasonic system. The ultrasonic waves are generated by pulsed laser and remotely detected by the laser Doppler vibrometer.

including the total focusing method (TFM) and full waveform inversion, can be applied [15,16]. LUT was recently accommodated for the FMC data acquisition by alternatively scanning the generation and detection laser beams [17]. TFM was then applied for full-matrix ultrasonic imaging [17,18]. Consequently, the overall detection sensitivity and imaging contrast were remarkably enhanced compared with those of standard B-scan imaging.

Meanwhile, only the longitudinal wave and its direct scattering or the longitudinal-longitudinal wave is used for the full-matrix imaging with TFM, whereas other useful signals, including longitudinal-shear, shear-longitudinal, and shear-shear, are ignored. While it may work well for simple defects, those with a regular shape, TFM cannot handle complex defects that are irregular in shapes or steep in slopes. To this end, the other available information contained in the FMC data should also be efficiently explored. Thus, multi-mode TFM was proposed to exploit the useful signals completely [19]. However, the ray-trace based mechanism is still intrinsically limited in imaging complex defects despite improvements in the imaging contrast with multi-mode TFM. Therefore, advanced imaging methods are highly desired to create excellent images.

Deep learning techniques, which range from defects recognition and classification [20,21], beamforming [22,23], compressive sampling to speckle suppression [24], segmentation [25,26], and super-resolution imaging [27], have attracted considerable interest in ultrasonic NDE in the past decade. Different from the model-based ultrasonic imaging method, the deep learning method is a data-driven model, which fully extracts the features of ultrasonic signals and images to achieve the imaging of complex defects. The pixel-wise segmentation deep learning network enables the precise shape and size estimation of defects, thereby rendering the possibility for imaging detects with steep dipping or areas with strong velocity variations. However, only few studies on the application of deep learning to reconstruct laser-induced full-matrix ultrasonic imaging with elastic wave propagations are currently available.

To do that, the first attempt on the laser-induced ultrasonic full-matrix imaging of complex defects with deep learning is presented in this study. Laser Ultrasonic Phased Array (LUPA) was synthesized to accommodate the FMC data acquisition. The TFM images were then reconstructed as the inputs of deep learning network and the imaged defects were used as labels for the training. A visual geometry group-UNet (VGG-UNet) was then trained to predict the simulated or experimental TFM images. For proof-of-concept demonstrations, simulations and experiments are conducted to image complex defects to verify the effectiveness of the proposed method. The results show that VGG-UNet networks can generate high-quality ultrasonic images of complex defects with improved resolution and accurate details.
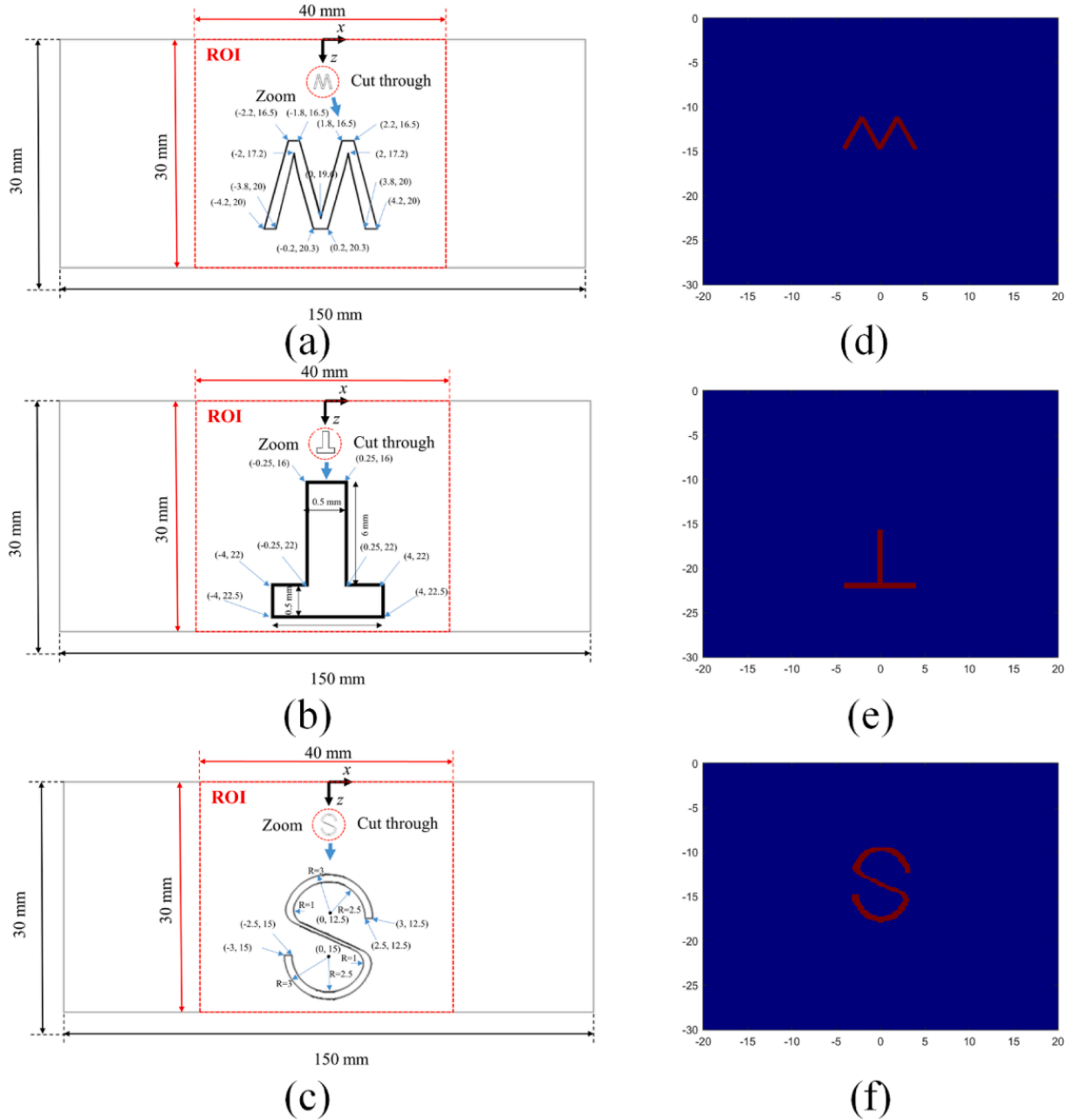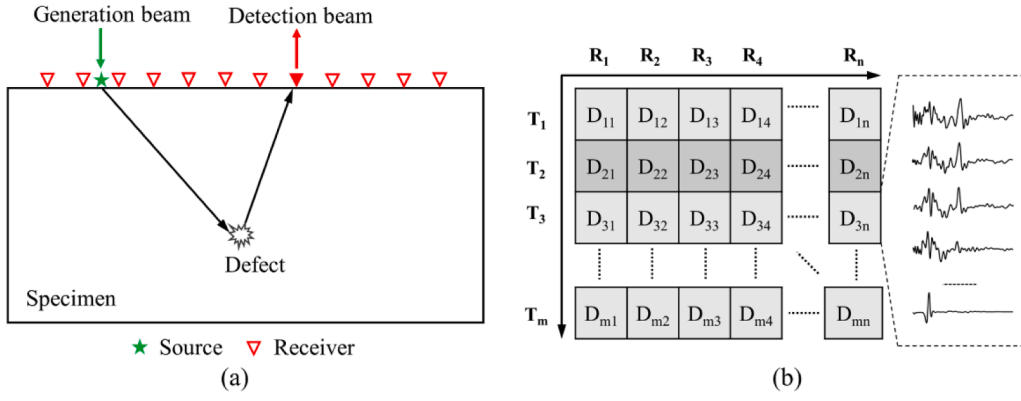
The rest of the paper is organized as follows. Section 2 presents the procedures for LUPA synthesis and FMC data acquisition. Section 3 outlines the architecture of VGG-UNet networks and the process of building datasets. Section 4 discusses the simulated and experimental results on the full-matrix imaging of complex defects with different shapes. Finally, Section 5 summarizes the discussions and future works.

2. LUPA synthesis and FMC data acquisition

This section presents an all-optical system for the LUPA synthesis. A pulsed laser was employed for the thermoelastic generation of ultrasonic waves, and a laser vibrometer was used for the detection of back-scattered waves based on the Doppler effect. The LU system records the time-trace signal from every source–receiver pair, and the FMC data were gathered through the scanning of pulse and detection laser beams.

2.1. All-optical setup for the generation and detection of ultrasonic waves

Fig. 1 illustrates the setup of an all-optical system for the generation and detection of ultrasonic waves. The specimen under test is an aluminum block embedded with an irregular defect. A compact Q-switched pulsed laser (Quantel Ultra100, France) with a wavelength of 1064 nm and a pulse duration of 7 ns was used to excite the ultrasonic waves. The pulse energy was set to 0.5 mJ to operate in the thermo-elastic regime with a repetition frequency of 20 Hz. The pulsed laser beam was first expanded from 3 mm to 12 mm in diameter and then focused into a cylindrical line with a lateral size of approximately 0.2 mm for the efficient generation of ultrasonic waves. A laser vibrometer (633 nm, Polytech GmbH, Germany) comprising an optical head (OFV-505) and a digital controller (OFV-5000) was used to acquire the

Fig. 3. The geometrical configurations of the samples under test. Samples are cut with (a) M-shaped, (b) inverse *T*-shaped and (c) S-shaped defects. (d-e) shows the schematic of the training label for (d) "M", (e) "T", and (f) "S" defects.

backscattered ultrasonic waves upon reaching the specimen surface. The optical head was inclined to facilitate guiding of the pulsed laser beam. The detection laser beam was also focused on a circular spot with a diameter of 0.1 mm. Out-of-plane ultrasonic signals were recorded as a function of time (*t*), namely time-trace signals, which were then pre-amplified (ZFL-500LN, Mini-Circuits, USA) and stored in a digital oscilloscope (Teledyne Lecroy HDO6054, USA). The time-trace signals were averaged by 20 times before storage to improve the signal-to-noise ratio.

2.2. LUPA synthesis and FMC data acquisition

Fig. 2 schematically depicts the synthesis of LUPA and the process for FMC data acquisition. Herein, the LU system served as a source–receiver pair. Unlike the piezoelectric counterpart where the source and receiver are overlapping, the excitation (green star) and detection (red triangle) positions of LU pairs can be individually arranged. For convenience, data trace D_{ij} was defined as the time-trace signal collected from one source–receiver pair, where i and j indicate the indexes of source and receiver, respectively. FMC data can then be obtained by gathering the data traces from every source–receiver pair. Different from a piezo-electric ultrasonic phased array that conducts the simultaneous collection of data traces from all receivers for one emission, the LU receiver array is formed by scanning the detection laser beam across consecutive positions with a predefined pitch while maintaining the pulsed laser beam [Fig. 2(a)]. Consequently, one row of FMC data can be assembled when the scanning of detection laser beams is completed. Thereafter, the pulsed laser beam is moved to the next excitation position, and the detection laser beam is scanned again across all detection points. This process is repeated by scanning the pulsed laser beam, and LUPA can be readily synthesized to acquire the FMC data. Notably, the scanning of pulsed laser beams in this study was realized by moving the sample on a 1D stage instead because adjusting the pulsed laser and its accessorial optics for beam bending is difficult and was therefore kept stationary throughout the experimental measurements.

3. VGG-UNet for laser-induced ultrasonic full-matrix imaging

Multiple waves (longitudinal, shear, and surface waves) are simultaneously generated in LUT; among which, the shear wave mode is most efficiently excited. These characteristics contribute to the complexity of the propagation of waves; traditionally, reconstructing the imaging of defects using model-based ultrasonic imaging techniques is difficult. Therefore, a deep learning method is adapted for laser-induced full-matrix ultrasonic imaging. VGG-UNet is a U-shaped convolutional neural network with a VGG16 backbone, which can realize fast and precise pixel-wise prediction using a scarce amount of training images [28]. Preparing enough dataset from practical NDT testing is also difficult despite the minimal requirements of VGG-UNet for training samples. Hence, a 2D finite element model was established to build a simulated dataset using COMSOL Multiphysics 5.3a. The simulated data from physics-based models can be used in improving the performance of a data-driven algorithm [29]. The trained network enables the precise shape and size estimation of defects, which is an excellent candidate to yield high-quality images for complex defects.

3.1. Governing equations for laser-induced ultrasonic waves

For the thermoelastic generation of laser ultrasonic waves in a solid material, the governing equations can be described as follows [30]:

$$\rho C_{\mathrm{p}}\frac{\partial T}{\partial t} - k\nabla^2 T = q_0 \tag{1}$$

$$\mu\nabla^2\mathbf{u} + (\lambda+\mu)\nabla(\nabla\cdot\mathbf{u}) - (\rho\ddot{\mathbf{u}} + \zeta\dot{\mathbf{u}})] = \alpha(3\lambda+2\mu)\nabla T, \tag{2}$$

Table 1
The material parameters of aluminum specimen.

ρ	λ	μ	κ	C_p	α
2700 kg/m³	51 GPa	26 GPa	238 W/(m·K)	900 J/(kg·K)	2.3 × 10^{-5} K⁻¹

where T is the temperature distribution, ρ is the density, C_{p} is the heat capacity, k is the thermal conductivity, and t is the time; λ and μ are the Lamé constants, ζ is the acoustic damping coefficient, and α is the thermal expansion coefficient.

Notably, a Q-switched Nd:YAG laser was used in the study. Therefore, the heat source q_0 can be approximated as Gaussian in both spatial and temporal distributions as:

$$q_0 = A_0 I e^{-A_{\mathrm{c}}|y|}\cdot e^{\left(\frac{x-x_0}{\sigma_0}\right)^2}\cdot e^{\frac{-2t^2}{t_0^2}}\left(\frac{t}{t_0}\right)^3, \tag{3}$$

where A_0 is the optical absorptivity of the specimen, I is the laser intensity, A_{c} is the optical attenuation coefficient along the depth, x_0 and σ_0 are the center and half irradiation width of the pulsed laser source, respectively, and t_0 is the rise time of the laser pulse.

3.2. Dataset

A dataset consisting of 204 cases of a full wavefield of laser-induced ultrasonic waves was generated in this study for each complex defect, including "M," inverse "T," and "S" shapes. The dimension of the aluminum block is 135 mm × 30 mm, and the defects are respectively shown in Fig. 3(a–c). The material parameters of the aluminum used in this study are listed in Table 1. A 2D finite element model was established using COMSOL, which employs *Heat Transfer in Solid* and *Solid Mechanics* to model the generation, propagation, scattering, and other wave dynamics of the laser-induced ultrasonic waves. The two physical modules were coupled with *Thermal Expansion* and *Temperature Coupling* interfaces. For simplicity, the pulsed laser source was approximated with a volumetric heat source, which is Gaussian distributed over time and along the *x*-direction as expressed in Eq. (3). The laser radiation was absorbed in a superficial layer, and the optical penetration depth was in the magnitude of nanometers. The rising time and optical penetration depth of the heat source were respectively set to 7 ns and 100 nm to accommodate the laser-induced ultrasonic waves in the experiments. The defects were defined by removing the materials in solid and assigning the resulting domain to air. The model used a fine mesh with size $\lambda/20$ (λ being the wavelength of shear wave) within the heated region to resolve its pressure and temperature gradients accurately. A coarse mesh with size $\lambda/10$ was employed for the other domains. Triangular elements were also applied to discretize the acoustic pressure and temperature. Perfect matched layers were used to absorb the outgoing waves. The model employed a time-dependent solver to study the acoustic pressure field in the time domain. The time step was set to 0.1 and 10 ns respectively during the pulse duration and rest period. The particle velocity was recorded over time at the receiver positions via *Domain Point Probe*. An array of 65 sources and 64 receivers was configured in the simulation, with the array center aligning to that of the defect. The sources and receivers were equally spaced with a pitch of 1 mm and were offset by 0.5 mm. Consequently, the coordinates of the sources and receivers along the *x*-direction are $T = -32$ mm: 1 mm: 32 mm and $R = -31.5$ mm: 1 mm: 31.5 mm, respectively. The FMC data were collected by simultaneously recording the time-trace signals at all receivers for each pulse laser shot and sweeping the heat source step-by-step through a parametric study.

The ultrasonic waves were excited with low pulse energy for non-destructive and repetitive operations, and therefore the sensitivity of optical detection was relatively low. Thus, the measured signals were
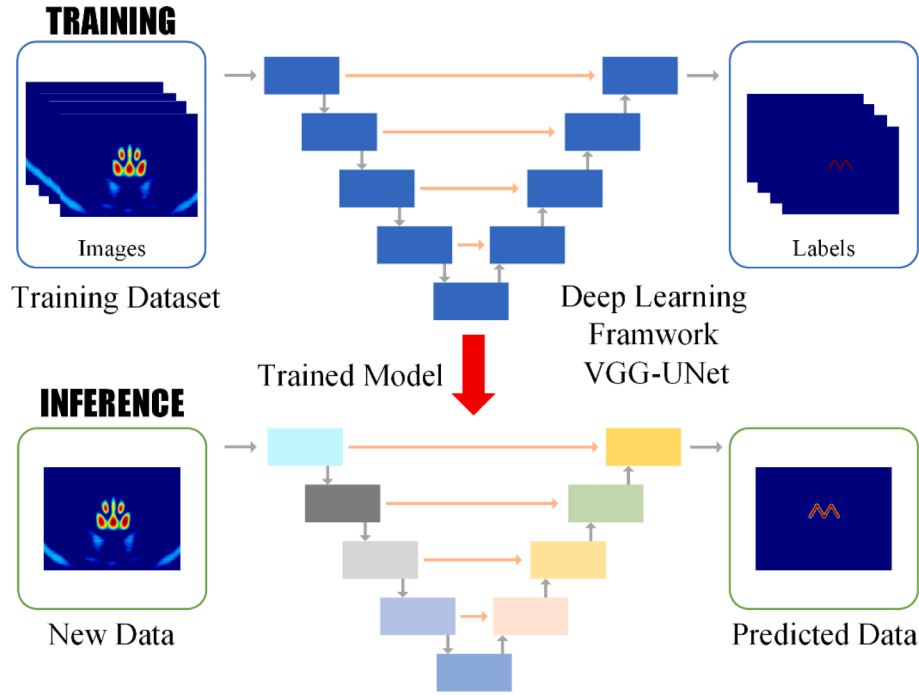
Fig. 4. The schematic principle and configuration of VGG-UNet.

first filtered to improve the signal-to-noise ratio before the application of the full-matrix imaging algorithms. Hilbert transform was adopted in this study according to the central frequency and − 6 dB bandwidth of the laser-induced ultrasonic waves, which were 1.5 and 2.0 MHz, respectively. Meanwhile, surface Rayleigh waves were eliminated using time gating and zero padding method as they are much stronger than their bulk counterparts and will substantially deteriorate the imaging contrast. The time gating width was 1.5 us according to the measured data. The full-matrix laser-induced ultrasonic signals are used to reconstruct the ultrasonic images by TFM. The region of interest is 40.1 mm × 30.1 mm, with the center of the imaging region aligning to that of the aluminum block, corresponding to a 401 × 301 pixel image. Each pixel represents 1 mm. The TFM images are generated as training inputs while the defects are served as labels for the training, as shown in Fig. 4.

Each TFM image is reconstructed from the acquired FMC data, which includes 32 transmitters and 64 receivers, to balance the simulation time and the number of datasets. Moreover, the specific defect is randomly placed in the block. All simulations are performed in COMSOL, which runs on a Windows 10 platform, with 2.3 GHz Intel Xeon Gold 5218 CPUs, 256 GB RAM, and NVIDIA GeForce RTX 2080 Ti. Finally, a total number of 204 ultrasonic images are simulated for each kind of defect. Among them, 122 ultrasonic images are generated as training inputs. The number of validation sets is 41, and 41 images are used for the test set. The validation dataset is used to tune the parameters, including the depth of encoding layer, batch size, and the learning rate of the optimizer, while the test set is used to assess the generalization capability of VGG-UNet.

3.3. VGG-UNet network

TFM imaging cannot handle complex defects. Therefore, a VGG-UNet is adopted to reconstruct the details of defects by using the TFM images. In other words, a supervised deep learning network is adopted to find an optimal mapping between TFM images and defects, which can be given by

$$h^* = \underset{h}{\mathrm{argmin}} \, \underset{(x,y)}{D} \left[L(h(x,y),y) \right] \tag{4}$$

where $x \in X$ is a TFM image in the input data, $y \in Y$ is a defect image in the output data, h represents X→Y mapping, L is the loss function, and D is a limited dataset. The mapping space H comprised a fixed VGG-UNet structure with parameter space Θ. Therefore, the search for h^* leads to find the optimal parameters θ^*. Parameter θ^* is adjusted in the training process through the guidance of the label. The loss function used to train the network is the binary cross-entropy loss given by

$$L_{binary} = -\left[Y\log\left(\hat{Y}\right) + (1 - Y)\log\left(1 - \hat{Y}\right) \right] \tag{5}$$

where $\hat{Y}$ is a predicted image. Furthermore, the optimization used for training the deep learning model is Adam, which accelerates the training process.

In order to reconstruct the details of complex defects, a deep learning ultrasonic imaging model was proposed based on UNet network, as shown in Fig. 4. The structure of UNet network is similar to that of the letter "U". Downsampling is firstly carried out through convolution and pooling. Then the feature maps of upsampling layer is extracted through deconvolution, to which that the downsampling features are skip-connected and concatenated for preserving the accuracy of defect shape, size and position. Finally, the size of inferred output images is consistent with the input image. The network capturing feature maps by up-down sampling can also be called encoder-decoder model, which can realize the extraction of some basic features of laser-induced ultrasonic images. However, the conventional UNet network consists of five convolution layers, which cannot learn and predict the advanced features of ultrasonic images. For the sake of increasing the data depth of ultrasonic images, the VGG16 is applied to replace the left encoder layers of UNet, which can increase the convolution layers of each downsampling blocks. What's more, the adopted VGG network does not break the skip-connection rule of UNet. And the pooling layer of each blocks is changeless to ensure that image size exported by each encoder blocks is not affected. The network achieved in this study is designed in Keras. The programming language is Python.
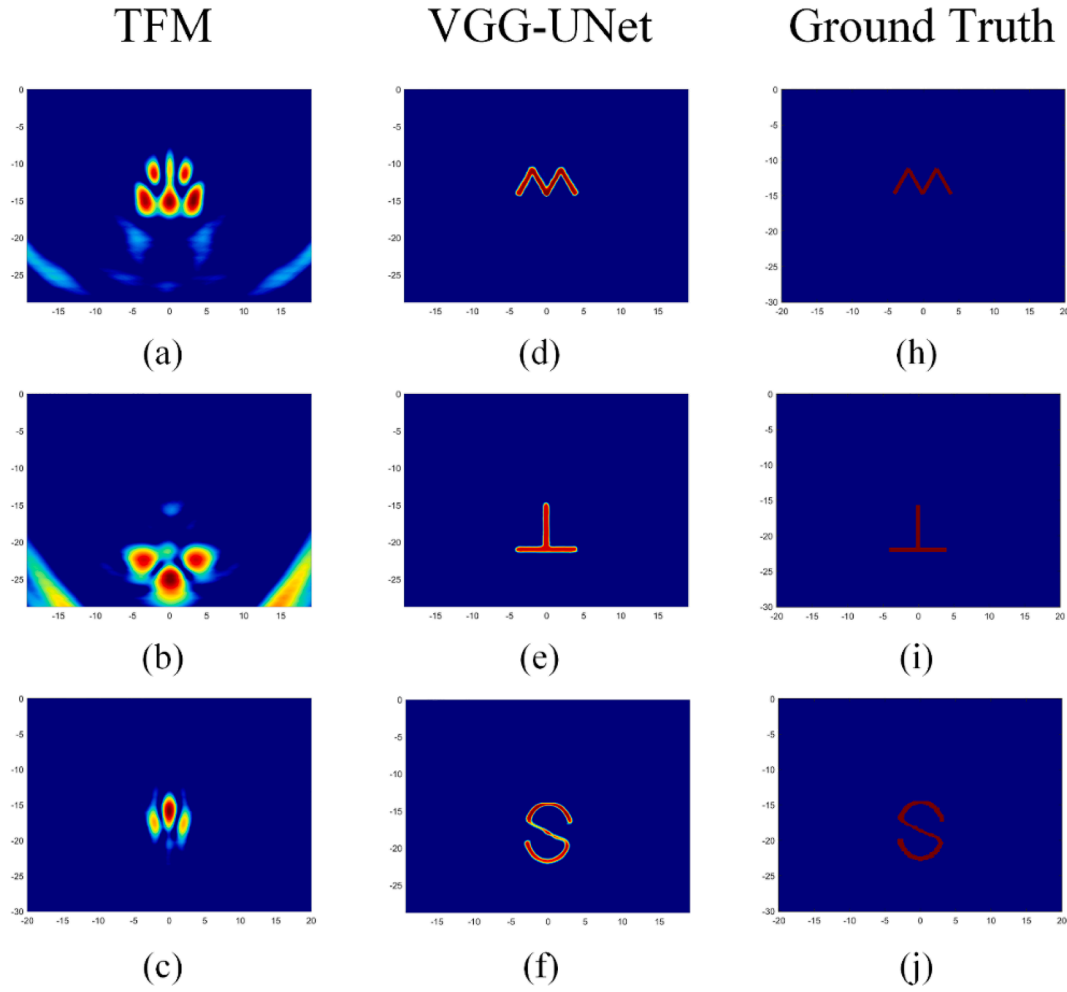
Fig. 5. The simulated results of laser induced full-matrix ultrasonic imaging. (a-c) The ultrasonic images reconstructed by TFM for (a) "M", (b) inverse "T", and (c) "S" defects, respectively. (d) "M", (e) inverse "T", and (f) "S" defects are reconstructed by VGG-UNet. (h-j) show the ground truths.

4. Results

Simulations and experiments for the laser-induced ultrasonic full-matrix imaging of complex defects were performed to verify the effectiveness of the proposed method. For comparison, the simulated and measured data were also employed with TFM. Results showed that VGG-UNet remarkably improved the imaging performance.

4.1. Verification of simulation data

4.1.1. Samples with different shape defects

For the proof-of-concept demonstrations, three samples were cut with representative "M" inverse "T" and "S" shaped defects as shown in Fig. 3. "M" and inverse "T" shapes were both created to represent the general case with steep boundaries, while "S" shape was created to represent the general case of curved boundaries.

The TFM algorithm is firstly applied for the full-matrix imaging as shown in Fig. 5(a)–(c). Fig. 5(a) shows that only the five corners of the M defect can be observed, which provides a rough indication of the defect and its location. Fig. 5(b) reveals that the vertical and horizontal boundaries are missing, and the defect profile cannot be reproduced. Fig. 5(c) shows that the curved upper contour of the "S" shape cannot be completely reconstructed, while the bottom is totally missing. These results readily confirm that TFM cannot handle complex defects that are irregular in shapes, steep in slopes, or curved boundaries.

The reconstructed images are then fed into the trained VGG-UNet.

The predicted images are shown in Fig. 5(d)–(f). For comparison, Fig. 5(h)–(j) shows the images of ground truths. As can be seen, they are in good agreement, in which the vertical edges, horizontal steps, and curved boundaries are successfully reconstructed regarding shape and location. These results readily support claims for the laser-induced ultrasonic imaging of complex objects. Compared with the TFM, VGG-UNet can generate remarkably accurate results and thus provide substantially meaningful information regarding the complex defect, such as the shape, orientation, and length, which are crucial for the judgment and prediction of defect formation and development.

4.1.2. Samples with different dimension and orientation defects

In this section, three samples with M-shaped defects of different dimension and orientation were used to verify the feasibility of the proposed deep learning model. Another 102 cases were added to the training dataset, which consist of samples with M-shaped defects of random dimension, orientation and position. Afterwards, the new training dataset was used to re-train the VGG-UNet with fine-tuning strategy, of which the backbone parameters were frozen. Eventually, the measured echo signals of three samples with representative defects were reconstructed by VGG-UNet. The defects in three samples took the "M" shaped defect shown in Fig. 3(a) as a reference, which were rotated by 45°, zoomed in twice, and rotated by 90°, respectively. Meanwhile, the dimension, rotation angle and position of the defects in the three samples were confirmed to be completely different from those in the training set.
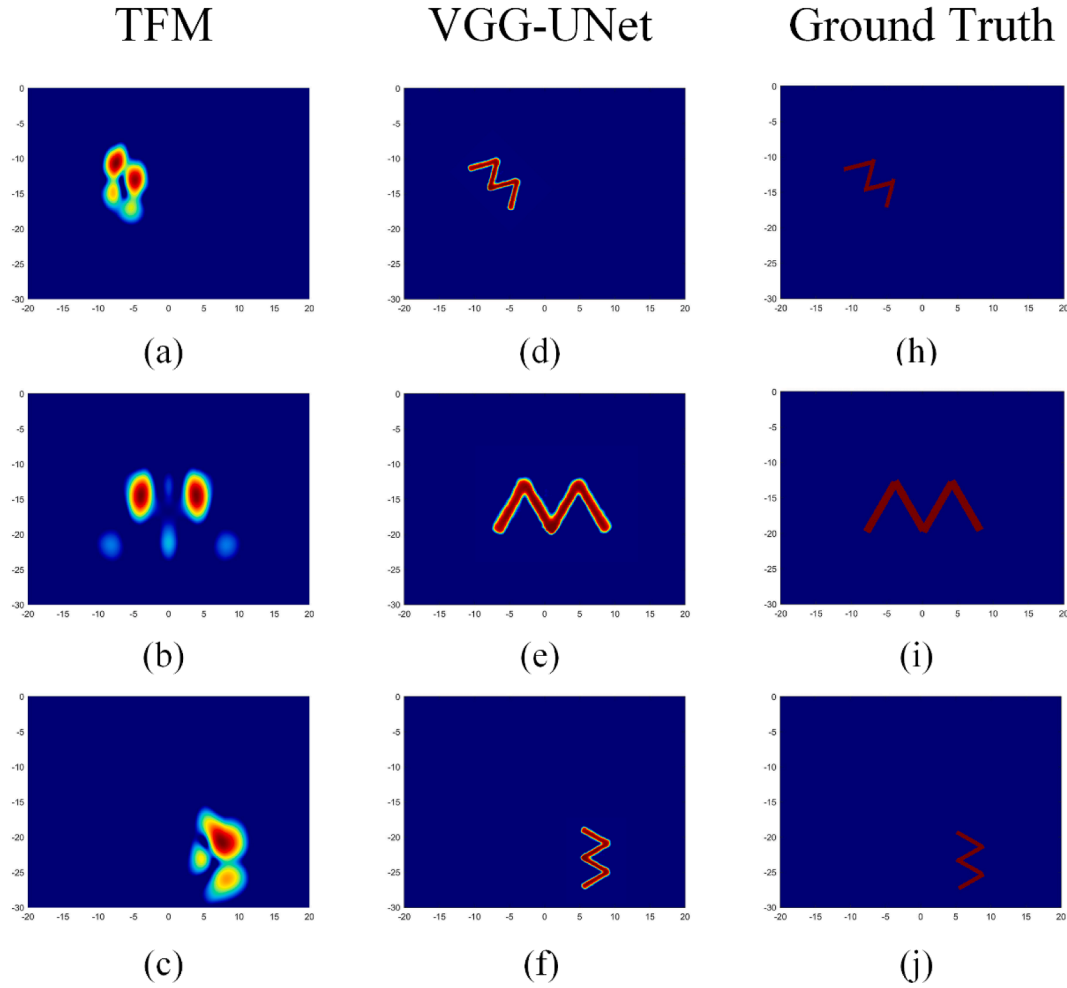
Fig. 6. The simulated results of laser induced full-matrix ultrasonic imaging. (a-c) The ultrasonic images reconstructed by TFM for "M" shaped defects which are (a) rotated by 45°, (b) zoomed in twice, and (c) rotated by 90°, respectively. (d-f) Defects are reconstructed by VGG-UNet. (h-j) show the ground truths.
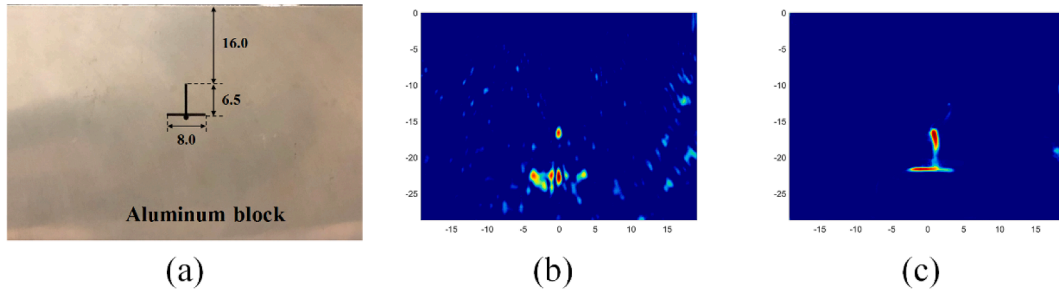

Fig. 7. The experimental results of laser induced full-matrix ultrasonic imaging. (a) The photography and geometrical configurations of the sample for experiment. (b) The defect of inverse "T" is reconstructed by (b) TFM and (c) VGG-UNet, respectively.

The TFM algorithm is firstly applied to the acquired FMC data and the images are shown in Fig. 6(a)–(c). The ultrasonic imaging results show that the boundaries of defects are vague. The corners of defect even cannot be observed, when the defects are rotated by some degrees. However, the laser ultrasonic images enhanced by the re-trained VGG-UNet show clearly vertical, horizontal and sloping edges as shown in Fig. 6(d)-(f). Meanwhile, the defects can be located precisely. They are in good agreement with the ground truth shown in Fig. 6(h)-(j).

The simulation results also illustrate that VGG-UNet model can significantly improve the effect of ultrasonic imaging, which can extract accurate information about boundaries and vertices. What's more, the VGG-UNet model thrives on the richness of the training dataset. In order

to drive more accurate prediction across a wider application scenario, richer datasets need to be built.

4.2. Application to experimental data

4.2.1. Ultrasonic imaging of T-shaped defect using deep learning

A sample made of aluminum blocks with dimensions 200 mm × 50 mm × 100 mm was used to further verify the feasibility of the proposed method. A through-thickness defect of inverse "T" shape was created through wire cutting. The geometrical configurations of the sample and its photograph are shown in Fig. 7(a) for clarity.

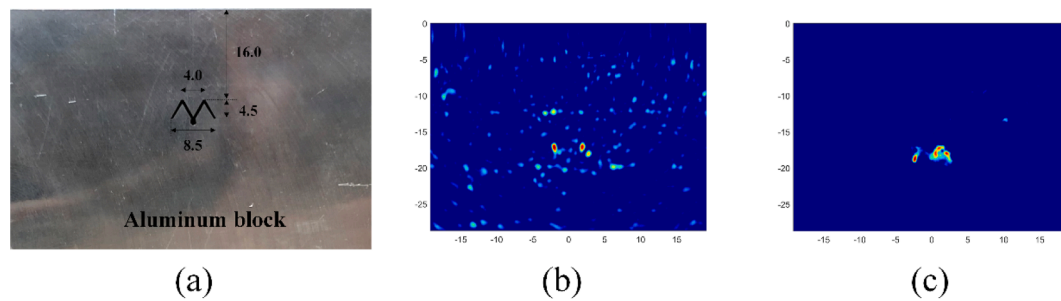A 1D LUPA was synthesized during FMC data acquisition as

Fig. 8. The experimental results of laser induced full-matrix ultrasonic imaging. (a) The photography and geometrical configurations of the sample for experiment. (b) The defect of "M" is reconstructed by (b) TFM and (c) VGG-UNet, respectively.

presented in Section 2.2. An array of 65 sources and 64 receivers was configured with an array center similar to that of the defect. The sources and receivers were equally spaced with a pitch of 1 mm and were offset by 0.5 mm. The sampling rate was set to 100 MHz during the experiments, and the recording time length was 30 μs. The central frequency and − 6 dB bandwidth of the laser-induced ultrasonic waves were 1.8 and 2.0 MHz, respectively, according to the measured data.

Fig. 7(b) shows the measured ultrasonic image reconstructed by TFM. The imaging result reveals that the defect tips are well imaged, indicating the existence of a defect. However, the vertical and horizontal boundaries are missing, and the defect profile cannot be reproduced, the same as that observed in the simulation. The TFM image is then fed into the trained VGG-UNet, and the predicted image is shown in Fig. 7(c). The experimental result indicates that the vertical edge and horizontal step are well reconstructed considering shape and location. Nevertheless, the imaging performance of the experimental image is slightly poorer than the simulation. Compared with the noise-free simulation result, the experimental image was degraded by the notable background artifacts in the measured image, which are remarkable and displayed a wave-like pattern. The result also indicates that the VGG-UNet trained by the simulation dataset is still valid for experimentally acquired FMC data. The trained VGG-UNet also exhibits good generalization behavior, as well as the robustness on the experimental data suffered noise.

4.2.2. Ultrasonic imaging of M-shaped defect using deep learning

Experiments were also carried out for the laser-induced ultrasonic full-matrix imaging of arbitrarily irregular defect to further prove the imaging capability of the proposed method. Sample 2 with an M-shaped defect was used, and the same procedures for the acquisition of experimental FMC data were adopted. TFM and VGG-UNet were applied for the adopted FMC data. Fig. 8(b) and (c) show the imaging results from sample 2, respectively. Compared with the noise-free simulation result as shown in Fig. 5(a), the experimental image was degraded by the remarkable background artifacts, as shown in Fig. 8(b). Only two corners of the M-shaped defect can be clearly seen in the TFM image, thus providing little indication of the defect and its location. However, most pieces of information about this irregular defect regarding its profile and location were captured and reproduced by the VGG-UNet as shown in Fig. 8(c), which shows that even in the absence of noise and the imaging performance of VGG-UNet ultrasonic imaging is better than that of TFM. These results once again validate the effectiveness of the proposed method for imaging complex defects.

5. Summary and discussions

In this study, the synthesized LUPA is proposed to achieve the non-contact detection of complex defects, which outperformed its traditional piezoelectric counterpart considering the fully non-contact generation and detection of ultrasonic waves and the flexibility on array design and configuration. The proposed method would be applicable for NDT applications in hazardous environments (high temperature,

pressure, or toxicity) and online monitoring, such as coating fabrication and additive manufacturing, due to its couplant-free and non-destructive nature. This technique can also easily accommodate complex geometries, rotating components, large inspection areas, and places of limited access. Furthermore, a VGG-UNet ultrasonic imaging model is trained to improve the laser-induced ultrasonic full-matrix imaging, which can overcome the shortcomings of low detection sensitivity and complicated wave mode conversion of laser ultrasound. Additionally, the simulation and experimental results exhibited excellent imaging performance of VGG-UNet in reproducing the defect characteristics, such as shape, size, and location, which yielded accurate results and quantitative information regarding the defect by learning advanced information from the ultrasonic images.

Considering the promising potential of the proposed method, ongoing work will be continued toward its practical applications as follows. (1) While the present work reveals the feasibility of the proposed method in 2D homogenous media, further studies are continuously conducted for its application in 3D anisotropic media and multilayer materials. (2) The optical detection sensitivity should be improved by increasing the power of the detection laser and optimizing the collection of backscattered light. (3) The long period for FMC data acquisition, which originated from the low repetition rate of the generation laser and the slow mechanical scanning, should be addressed. The acquisition time can be significantly reduced using a high repetition rate pulsed laser and Galvo scanning, thus contributing to the applicability of the technique for online process monitoring. (4) Limited by simulation time and experimental conditions, the application scenarios are restricted by the limited datasets. More efficient dataset establishment methods are worthy of research, so that the method can be used with a wider range.

All in all, integrating the LUPA and deep learning model is an attractive and promising method for the inspection of complex defects in scenarios where a conventional phased array is inapplicable. This technique can help explain and optimize the manufacturing process and provide information for the early detection of defects to assure the successful synthesis of safety–critical components.

Declaration of Competing Interest

The authors declare that they have no known competing financial interests or personal relationships that could have appeared to influence the work reported in this paper.

Data availability

Data will be made available on request.

Acknowledgments

References

[1] W.S. Gan, Acoustical Imaging: Techniques and Applications for Engineers, John Wiley & Sons, Chichester, 2012.

[2] B.W. Drinkwater, P.D. Wilcox, Ultrasonic arrays for non-destructive evaluation: A review, NDT & E. Int. 39 (7) (2006) 525–541.

[3] M. Felice, Z. Fan, Sizing of flaws using ultrasonic bulk wave testing: a review, Ultrasonics 88 (2018) 26–42.

[4] V. Marcantonio, D. Monarca, A. Colantoni, M. Cecchini, Ultrasonic waves for materials evaluation in fatigue, thermal and corrosion damage: A review, Mech. Syst. Sig. Process. 120 (2019) 32–42.

[5] C.B. Scruby, L.E. Drain, Laser Ultrasonics: Techniques and Applications, Adam Hilger, 1990.

[6] B. Park, H. Sohn, P. Liu, Accelerated noncontact laser ultrasonic scanning for damage detection using combined binary search and compressed sensing, Mech. Syst. Sig. Process. 92 (2017) 315–333.

[7] Z. Tian, S. Howden, Z. Ma, W. Xiao, L. Yu, Pulsed laser-scanning laser Doppler vibrometer (PL-SLDV) phased arrays for damage detection in aluminum plates, Mech. Syst. Sig. Process. 121 (2019) 158–170.

[8] P. Grasland-Mongrain, Y. Lu, F. Lesage, S. Catheline, G. Cloutier, Generation of shear waves by laser in soft media in the ablative and thermoelastic regimes, Appl. Phys. Lett. 109 (22) (2016), 221901.

[9] C. Pei, T. Fukuchi, H. Zhu, K. Koyama, K. Demachi, M. Uesaka, A study of internal defect testing with the laser-EMAT ultrasonic method, IEEE Trans. Ultrason. Ferroelectr. Freq. Control 59 (12) (2012) 2702–2708.

[10] J.P. Monchalin, R. Heon, Broadband optical detection of ultrasound by optical sideband stripping with a confocal Fabry-Perot, Appl. Phys. Lett. 55 (1989) 1612–1614.

[11] J. Steckenrider, T. Murray, J. Deaton, J. Wagner, Sensitivity enhancement in laser ultrasonics using a versatile laser array system, J. Acoust. Soc. Am. 97 (1995) 273–279.

[12] R.J. Dewhurst, Q. Shan, Optical remote measurement of ultra-sound, Meas. Sci. Technol. 10 (11) (1999) 139–168.

[13] C. Holmes, B.W. Drinkwater, P.D. Wilcox, Post-processing of the full matrix of ultrasonic transmit-receive array data for non-destructive evaluation, NDT & E. Int. 38 (8) (2005) 701–711.

[14] H. Wu, J. Chen, K. Yang, X. Hu, Ultrasonic array imaging of multilayer structures using full matrix capture and extended phase shift migration, Meas. Sci. Technol. 27 (4) (2016), 045401.

[15] C. Holmes, B.W. Drinkwater, P.D. Wilcox, The post-processing of ultrasonic array data using the total focusing method, Insight 46 (11) (2004) 677–680.

[16] C. Holmes, B.W. Drinkwater, P.D. Wilcox, Post-processing of the full matrix of ultrasonic transmit–receive array data for non-destructive evaluation, NDT & E. Int. 38 (8) (2005) 701–711.

[17] T. Stratoudaki, M. Clark, P.D. Wilcox, Laser induced ultrasonic phased array using full matrix capture data acquisition and total focusing method, Opt. Express. 24 (19) (2016) 21921–21938.

[18] J. Chen, J. Xiao, D. Lisevych, Z. Fan, Laser-Induced Full-Matrix Ultrasonic Imaging of Complex-Shaped Objects, IEEE Trans. Ultrason. Ferroelectr. Freq. Control 66 (9) (2019) 1514–1520.

[19] J. Zhang, B.W. Drinkwater, P.D. Wilcox, A.J. Hunter, Defect detection using ultrasonic arrays: The multi-mode total focusing method, NDT & E. Int. 43 (2010) 123–133.

[20] F.W. Margrave, K. Rigas, D.A. Bradley, P. Barrowcliffe, The use of neural networks in ultrasonic flaw detection, Measurement 25 (2) (1999) 143–154.

[21] Y. Lu, L. Ye, Z. Su, L. Zhou, Artificial neural network (ANN)-based crack identification in aluminum plates with Lamb wave signals, J. Intell. Mater. Syst. Struct. 20 (1) (2009) 39–49.

[22] A.C. Luchies, B.C. Byram, Deep neural networks for ultrasound beamforming, IEEE Trans. Ultrason. Ferroelectr. Freq. Control. 37 (9) (2018) 2010–2021.

[23] B. Luijten, R. Cohen, F.J. De, Bruijn, Adaptive Ultrasound Beamforming Using Deep Learning, IEEE Trans. Ultrason. Ferroelectr. Freq. Control. 39 (12) (2020) 3967–3978.

[24] D. Hyun, L.L. Brickson, K.T. Looby, Beamforming and Speckle Reduction Using Neural Networks, IEEE Trans. Ultrason. Ferroelectr. Freq. Control. 60 (5) (2019) 898–910.

[25] M. Amiri, R. Brooks, H. Rivaz, Fine-Tuning U-Net for Ultrasound Image Segmentation: Different Layers, Different Outcomes, IEEE Trans. Ultrason. Ferroelectr. Freq. Control. 67 (12) (2020) 2510–2518.

[26] A.A. Ijjeh, S. Ullah, P. Kudela, Full wavefield processing by using FCN for delamination detection, Mech. Syst. Sig. Process. 153 (2021), 107537.

[27] K.G. Brown, D. Ghosh, K. Hoyt, Deep Learning of Spatiotemporal Filtering for Fast Super-Resolution Ultrasound Imaging, IEEE Trans. Ultrason. Ferroelectr. Freq. Control. 67 (9) (2020) 1820–1829.

[28] Y. Mei, H. Jin, B. Yu, E. Wu, K. Yang, Visual geometry Group-UNet: Deep learning ultrasonic image reconstruction for curved parts, J. Acoust. Soc. Am. 149 (5) (2021) 2997–3009.

[29] D. Patel, R. Tibrewala, A. Vega, L. Dong, Circumventing the solution of inverse problems in mechanics throughdeep learning: Application to elasticity imaging, Comput. Methods Appl. Mech. Eng. 353 (2019) 448–466.

[30] B. Xu, Z.H. Shen, X.W. Ni, J. Lu, Numerical simulation of laser-generated by the finite element method, J. Appl. Phys. 95 (4) (2004) 2116–2123.